Available online at www.sciencedirect.com

ScienceDirect

Physics Procedia 66 (2015) 232 – 241

Physics Procedia

C 23rd Conference on Application of Accelerators in Research and Industry, CAARI 2014

Cargo and Container X-Ray Inspection with Intra-Pulse Multi-Energy Method for Material Discrimination

Aleksandr Y. Saverskiy*, Dan-Cristian Dinca, J. Martin Rommel

American Science and Engineering, Inc., 829 Middlesex Turnpike, Billerica, MA 01821-3907, USA

Abstract

The Intra-Pulse Multi-Energy (IPME) method of material discrimination mitigates main disadvantages of the traditional "interlaced" approach: ambiguity caused by sampling different regions of cargo and reduction of effective scanning speed. A novel concept of creating multi-energy probing pulses using a standing-wave structure allows maintaining a constant energy spectrum while changing the time duration of each sub-pulse and thus enables adaptive cargo inspection. Depending on the cargo density, the dose delivered to the inspected object is optimized for best material discrimination, maximum material penetration, or lowest dose to cargo. A model based on Monte-Carlo simulation and experimental reference points were developed for the optimization of inspection conditions.

Keywords: cargo inspection; material discrimination; intra-pulse multi-energy; standing-wave structure; Monte-Carlo simulation

1. Introduction: Material discrimination based on interlaced dual-energy interrogation

Material discrimination capabilities have become a standard requirement for security cargo and container inspection systems. Typically it is achieved by employing an electron accelerator capable of interlaced dual-energy operation. The different attenuation of the two (rarely more) X-ray pulses of distinct energy provides the input data for identifying the type of material being inspected (Ogorodnikov and Petrunin, 2002). There are several limitations inherent in this approach. Using two pulses separated in time for producing one inspection data point effectively reduces inspection speed or the horizontal resolution of the resulting image. Moreover, the basic assumption of dual-

* Corresponding author. Tel.: +1-978-8700; fax: +1-978-262-8805.
E-mail address: asaverskiy@as-e.com

doi:10.1016/j.phpro.2015.05.030

energy inspection is that the pair of pulses probes the same region of cargo which is approximately true as long as the cargo moves slowly. At high cargo speeds, however, the distance between the regions sampled by the two pulses becomes significant. Fast systems operate at speeds up to 60 km/h and currently available dual-energy linacs operate at 400 pulses per second. This combination leads to substantial ambiguity in determining the type of material as the cargo moves 4 cm between the two pulses. Widening the beam aggravates partial volume effects limiting the material discrimination to large homogeneous objects.

High penetration, good material discrimination, low radiation dose to inspected object and environment are not only important parameters but also contradictory requirements. The optimal balance depends on the inspected object and often varies over the length of the scan. This has motivated the design of adaptive systems which adjust the X-ray source parameters in response to the interrogated object. The newest development addressing the issue is Intra-Pulse Multi-Energy Inspection, which was first described in "System and method for intra-pulse multi-energy inspection" by Arodzero et al. (2013). It also offers an effective solution for the abovementioned ambiguity problem by employing fast detectors capable of resolving the multi-energy structure of the X-ray pulse. However, creating an X-ray source optimal for intra-pulse multi-energy detection is a separate and challenging task. Analyses of specific requirements for the linac based X-ray source, novel solution for adaptive multi-energy linac and analyses of imaging parameters achievable with proposed X-ray source are discussed in this paper.

Nomenclature

$P_{av,max}$, $P_{p,max}$	maximum average and maximum pulse radio frequency (RF) source power
t_p	linac RF-pulse duration
P, P_H, P_L,	RF pulse power, necessary to provide acceleration to high *(H)* and low *(L)* energy level
f, f_H, f_L, f_{DE}	linac pulse repetition frequency (PRF), of high, low, and dual-energy mode
t_f	accelerator system filling constant
τ	time constant of RF-cavity
Q_0	unloaded quality factor of RF-cavity
ω	accelerating structure operation frequency
β, β_0	coupling coefficient and optimal coupling coefficient of RF-cavity
r	effective shunt impedance per unit length
L	accelerating system length
t, t_L, t_H	time starting from beginning of RF pulse, duration of low, and high energy sub-pulses
t_b, t_{bL}, t_{bH}	time when accelerating current is turned on, for low, and high energy level
W, W_H, W_L	electron beam energy, of high *(H)* and low *(L)* level.
I, I_H, I_L, I_n	electron beam current corresponding to high *(H)*, low *(L)* or n-th *(n)* energy level
S	figure of merit (FOM) for characterizing material discrimination quality
r_{steel}, $r_{plastic}$	detector response ratio of low energy to high energy for steel and plastic
$\sigma_{r_{steel}}$, $\sigma_{r_{plastic}}$	standard deviation for corresponding distribution of multiple samples.

2. Linac based X-ray source with intra-pulse energy modulation

2.1. Requirements for linac based adaptive multi-energy intra-pulse X-ray source

The goal for designing adaptive intra-pulse multi-energy X-ray source is to create a pulse profile, which achieves the best penetration or material discrimination depending on the type of cargo while preserving the highest possible scanning speed and optimizing dose to cargo and environment.

The inspection speed is mainly limited by maximum linac pulse repetition frequency (PRF). The pulse power necessary for accelerating electrons to high (HE) and low (LE) energy levels in combination with available average power of the RF-source limits the maximum PRF. As an example and for comparison purposes a dual-energy interlaced 6/4 MeV S-band linac powered with 2.6 MW/2.6 kW magnetron is used. In HE mode the accelerator

produces X-ray pulses with $t_p \approx 3.3$ μs and maximum PRF of $f_H \approx 300$ Hz (pps). Assuming that t_p remains the same for both energies of the dual-energy interlaced linac the maximum available frequency can be estimated from equation (1). In case $P_H = P_L$, $f_{DE} = ½ f_H$ (RF-source power remains constant for both pulses which is the case for RF-switches/regulators, manipulation of beam loading, accelerating field phase shifting). If $P_L = ½ P_H$, $f_{DE} = ⅔ f_H$ (e.g. RF-source power supply modulation provides different levels of microwave power, generated by the source).

$$f_{DE} \approx \frac{P_{av,max}}{P_H \cdot t_p \cdot \left(1 + P_L / P_H\right)} = \frac{f_H}{\left(1 + P_L / P_H\right)} \tag{1}$$

In intra-pulse dual-energy operation (Arodzero et al., 2013) the scanning frequency can be at least as high as for the high energy mode. This benefit comes at the expense of breaking the pulse into two sub-pulses (with decreased electron charge and X-ray flux). However, this disadvantage can be converted into a benefit by enabling adaptive adjustments of the sub-pulse's width, as will be shown later.

The effective use of the RF-power inside the pulse is also important for forming the best possible beam energy spectrum and flux characteristics which directly affect the system's the imaging performance. The actual electron beam pulse duration is shorter than the RF-source pulse by the accelerator system filling time t_f. Linacs used in security applications are frequently based on a standing-wave accelerating structure since it provides a higher gradient at short accelerating system lengths. A resonant system standing-wave structure approaches the steady-state only exponentially. It takes, for instance, 3.0 time constants τ for reaching 95% of the steady-state value. The time constant of the microwave resonator τ is defined as (Ginzton, 1957):

$$\tau = \frac{2Q_0}{\omega(1+\beta)} \tag{2}$$

The coupling coefficient β is part of the accelerating system design and typically chosen to avoid RF-power reflection from the accelerating structure when the beam is on. The value of τ for the referenced S-band accelerating structure ranges from 0.3 to 0.5 μs. Therefore, reaching 95% of the steady-state value can take up to 1.5 μs, almost half of the pulse duration mentioned above.

Energy gain in standing-wave structures is given by (Miller, 1986):

$$W = \frac{\sqrt{4\beta rLP}}{1+\beta}\left(1 - exp\left(-\frac{t}{\tau}\right)\right) - \frac{IrL}{1+\beta}\left(1 - exp\left(-\frac{t-t_b}{\tau}\right)\right) \tag{3}$$

For the referenced accelerating structure, the beam energy W vs. time t is shown as dotted line in Figure 1b with the assumption that both RF-power and injected beam are turned on at the same time (t_b=0) and $t_{f,95\%} \approx 1$ μs. The 6 MeV portion of the beam lasts about 1.8 μs. The front portion of the beam pulse can be used for intra-pulse material discrimination as described by Arodzero et al., (2013). However, the small difference in average values between front portion ($W_{(0.2\text{-}1.0)\ \mu s}$=4.7 MeV) and high energy part of the pulse (5.8 MeV) is not ideal for good material discrimination. This pulse structure is a result of a transient process and not optimal for both high and for low energy probing.

Requiring $\partial W/\partial t = 0$ leads to the optimal beam delay t_b that allows forming a beam pulse structure with constant energy over the pulse duration and effectively reduces the filling time (Miller, 1986):

$$t_b = \tau \cdot \ln\left(\frac{\sqrt{4\beta rLP}}{IrL}\right) \tag{4}$$

The optimal coupling coefficient β_0 eliminates RF-power reflection from the accelerating structure with the beam on and can be found by resolving steady state form of $\partial W/\partial\beta=0$ (Sobenin et al., 1999). The equation *(4)* then reduces to:

$$t_b = \tau \cdot \ln\left(\frac{2\cdot\beta_0}{\beta_0 - 1}\right) \qquad (5)$$

2.2. Linac concept with intra-pulse energy modulation

The distinction of the energy levels can be significantly improved if the accelerating current is modulated within the pulse as illustrated in Figure 1a. The linac shown in Figure 1a consists of the traditional elements but the electron gun provides a two-level injection current pulse into the accelerating system while the RF-power remains constant. Due to the different beam loading, the output pulse contains two distinct energy levels close in values to what the reference 6/4 MeV interlaced linac produces.

The implementation of this method for a standing-wave accelerator is shown in Figure 1b. The solid lines show electron beam energy (red) and current (blue). The LE portion of the pulse t_L = (0 - 1.5) μs has average energy W_L=3.9 MeV at I_L=370 mA and the HE portion t_H = (1.5 - 3.3) μs has average energy W_H=5.8 MeV at I_H=125 mA.

Being able to vary the time when the accelerating current switches to produce high energy level is an additional feature of the intra-pulse method which enables dynamic control of the flux and corresponding energy spectrum delivered to the inspected cargo and environment. However, the implementation of this capability with a standing-wave structure working in transient mode with long filling time has a significant drawback: the average energy of each portion changes with the length of the sub-pulse. That greatly complicates material discrimination as multiple-points or parametric calibration is required.

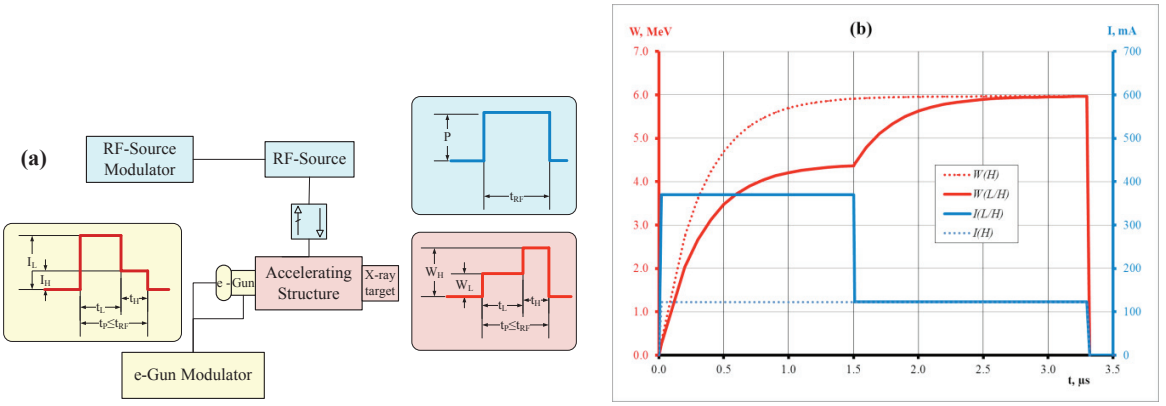

Fig. 1. (a) Block-diagram of intra-pulse dual-energy linac; (b) Electron beam energy and current for intra-pulse dual-energy operation (solid lined) and high energy pulse (dotted line) for interlaced operation.

The effective solution to this problem is using the optimal delay before supplying the beam current. Figure 2 shows the block-diagram of the linac and illustrates this technique. The standing-wave accelerating structure is designed to be optimally coupled for the low energy current while the value of the I_L is chosen to provide W_L. This energy remains constant over the sub-pulse duration if I_L is applied with delay t_{bL} with respect to the beginning of the RF pulse. The low energy current delay t_{bL} is given by equation (5). At the end of the low energy pulse the current is turned off. The RF-source power either remains constant or could be switched to a level chosen for creating the high energy pulse. The value of I_H is chosen to provide energy level W_H which also remains constant if the current is applied with delay t_{bH} counting from the end of low energy pulse. The value of t_{bH} can be found by employing a similar technique as was used for finding the optimal delay for the first sub-pulse t_{bL}. Equation (6) gives

the energy gain during the second sub-pulse assuming P_H=P_L. The first term of equation represents the input from the RF-generator, the second term is the decaying effect of the beam loading by I_L and the last term reflects the increasing beam loading during the second sub-pulse.

$$W_H = \frac{\sqrt{4\beta rLP}}{1+\beta}\left(1-exp\left(-\frac{t}{\tau}\right)\right)-\frac{I_L rL}{1+\beta}\left(1-exp\left(-\frac{t_L}{\tau}\right)\right)\cdot exp\left(-\frac{t-\left(t_{bL}+t_L\right)}{\tau}\right)- \\ -\frac{I_H rL}{1+\beta}\cdot\left(1-exp\left(-\frac{t-\left(t_{bL}+t_L+t_{bH}\right)}{\tau}\right)\right) \tag{6}$$

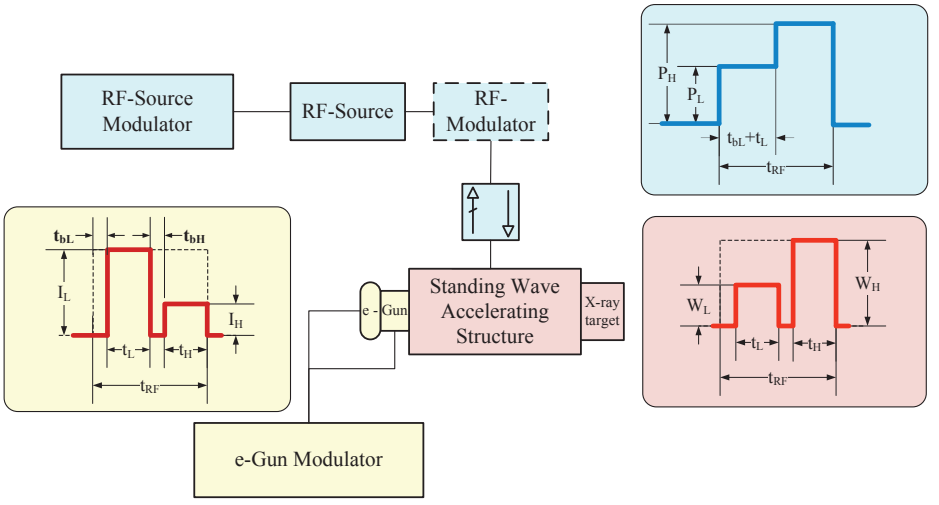

Fig. 2. Block-diagram of intra-pulse dual-energy linac with delayed application of electron beam currents corresponding to high and low energy levels.

Solving $\partial W_H/\partial t=0$ of equation (6) for t_{bH} with the condition that β_0 is chosen for low energy current, the high energy pulse delay t_{bH} is given by:

$$t_{bH} = \tau \cdot \ln\left(\frac{I_L}{I_H}\right) \tag{7}$$

The duration of sub-pulses (t_L and t_H) can be varied which enables dynamic control of the flux (dose) with corresponding energy delivered to cargo and environment. The energies within each sub-pulse remain constant as long as the low current is applied with t_{bL} delay and the high current with t_{bH} delay.

If the pulse has multiple energy levels, the required delay for n-th sub-pulse is given similarly by:

$$t_{bn} = \tau \cdot \ln\left(\frac{I_{n-1}}{I_n}\right) \tag{8}$$

The following assumptions were made when deriving these equations which also define the concept of linac operation.

- The coupling coefficient β_0 is chosen to be optimal for the first sub-pulse with current I_1 that has the highest value in the sequence of currents and creates the lowest energy W_1 in the sub-pulses sequence.
- The current values for the subsequent sub-pulses I_n have to be chosen in descending order. That will create an ascending order of beam energy levels W_n.
- After each sub-pulse, the current has to be turned off.

Each sub-pulse duration can still be varied enabling dynamic control of the flux at the corresponding energy within the macro-pulse. The energy within each portion will remain constant as long as the first current I_1 is applied with delay t_{b1} (defined by equation 5) and each following sub-pulse current I_n is applied with t_{bn} delay.

An example of linac operation with a dual-energy pulse created by applying the I_L and I_H currents with optimal delays is shown in Figure 3. Parameters of the linac are identical to those shown in the example in Figure 1b. The low energy current is applied with optimal delay of $t_{bL}\cong 0.34$ μs and is turned off at $t_L=1.45$μs. The high energy current is applied with delay of $t_{bH}\cong 0.36$ μs and is turned off at the end of the microwave pulse. The dotted line shows the high energy pulse created in transient mode for interlaced operation.

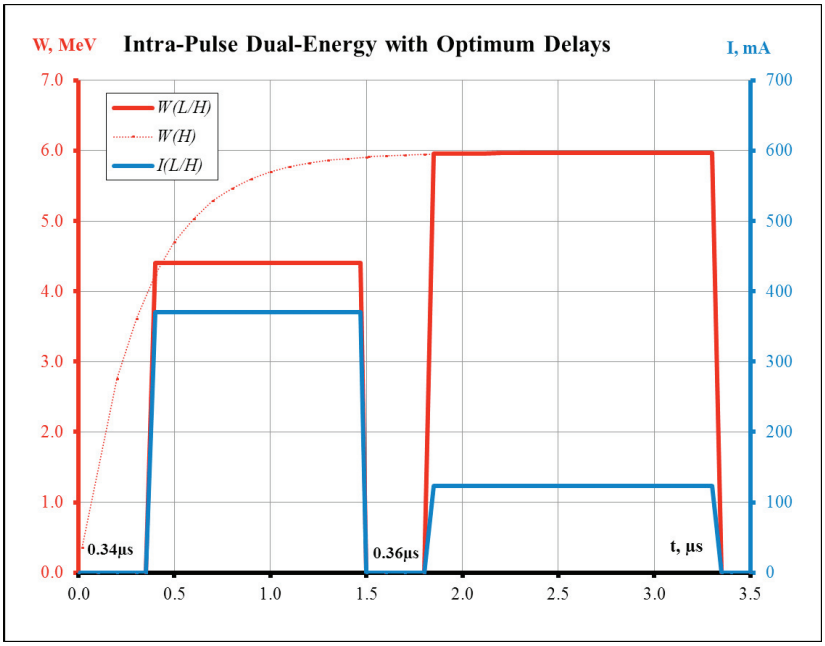

Fig. 3. Example of 6/4 MeV intra-pulse dual-energy linac with delayed application of low and high energy currents.

Frequently, using accelerating current modulation alone is not sufficient for creating desirable beam energy separation in intra-pulse dual-energy operation. The scenario that is shown in Figure 2 forms an ascending order of energy levels, each constant without a transition region. A corresponding ascending sequence of RF-power levels and descending sequence of injection current pulses needs to be applied. The coupling coefficient β_0 is still chosen optimal for the lowest energy sub-pulse. The low energy current delay t_{bL} is again given by equation (5). The high energy current delay t_{bH_a} can now be found by resolving the equation similar to (6) but with RF-generator power modulation:

$$t_{bH\_a} = \tau \cdot \left[\ln\left(\frac{I_L}{I_H}\right) + \ln\left(1 + \frac{2\cdot\beta_0}{\beta_0 - 1}\sqrt{\frac{P_H}{P_L} - 1}\right)\right] \tag{9}$$

3. Criteria and model for assessing imaging performance

Imaging performance is the leading concern when designing an X-ray Non-Intrusive Inspection (NII) system for scanning large objects such as cargo containers, trucks, or rail cars. Modern systems require high spatial resolution of 5 mm or better, penetration of 300 - 400 mm of steel equivalent (both per ANSI N42.46-2008), and good material discrimination. In addition, a small exclusion zone, low dose-to-cargo, and scan speeds greater than 0.3 m/s and up to 60 km/h are needed for some applications.

For testing the efficacy of the method described in the previous chapters the focus was on simulating the penetration, dose-to-cargo, and material discrimination capability. All these parameters depend strongly on the design details of a specific system such as X-ray beam opening angles, collimators, number of X-ray pulses per second from the linac, the scatter mitigation techniques applied, etc. In order to reduce the number of variables of the study, the system chosen was AS&E's OmniView Gantry (2010) modeled with different linac source parameters.

X-ray penetration and the source dose rate were simulated using Geant4 (Agostinelli et al., 2003). The dose-to-cargo is directly proportional to the dose rate of the source, estimated using Monte Carlo methods.

Material discrimination is achieved using the dual-energy method, widely used in the NII industry. Good descriptions of the method can be found in publications such as Ogorodnikov and Petrunin (2002), Liu and Tickner (2008), or Mandava et al (2009). The method involves a calibration process in which a set of materials with known atomic numbers and densities such as plastic, aluminum, steel, lead, tungsten, with different thicknesses are put between the source and detectors and the detector response for the high and low energy beam components is recorded. In normal operation mode, the inverse process takes place. Detectors are recording the high and low energy response to objects in the beam, and then algorithms are finding the closest candidate in terms of material type and thickness. An uncertainty is associated with the determination of the material type, depending on the system geometry, X-ray flux and energies and the number of samples (pulse pairs) used to make the determination. Figure 4a shows an example of experimental data obtained from a system operating with a low energy of 5.0 MeV and high energy of 7.5 MeV.

For each material, in this case Ultra High Molecular Weight polyethylene (UHMW PE) and steel, a calibration curve is created plotting the ratio of the detector response at low energy to the detector response at high energy as a function of material areal density. The one sigma bars are describing the width of the distribution of multiple samples of the same material and thickness, not the uncertainty associated with the ratio. The larger the spacing between the two calibration curves, the better the material discrimination that can be achieved. With a set confidence interval, for thicknesses of the two materials for which the calibration curves are closer and/or the uncertainty is larger, multiple samples need to be averaged to make a material identification.

A Figure of Merit (FOM) is defined as the separation between calibration curves (difference of low/high ratios) divided by the average of the distribution widths at a given material thickness.

$$S = \frac{\left| r_{steel} - r_{plastic} \right|}{\left(\frac{\sigma_{r_{steel}} + \sigma_{r_{plastic}}}{2} \right)} \qquad (10)$$

This FOM defines how well one can distinguish one material from the other. For a given pair of materials, in this case UHMW PE and steel (Figure 4b), it quantifies how many average standard deviations separate the two calibration curves.

Imaging performance was simulated for a source with the low energy segment energy of 3 MeV and peak beam current of 200 mA, the high energy segment was chosen to have energy of 6 MeV and peak beam current of 125 mA. The minimum pulse duration for each component was 0.3 μs. For a pulse rate of 300 Hz, delays were set at 0.43 μs for t_{bL} and at 0.71 μs for t_{bH}. The duration of the low energy pulse is varied from 0.3 μs to 1.89 μs and the duration of the high energy pulse is adjusted linearly, going from 1.89 microseconds, corresponding to the LE pulse of 0.3 microseconds, to 0.3 microseconds, corresponding to the LE pulse of 1.89 microseconds. The total dose rate,

penetration (Figure 5), and material discrimination FOM (Figure 6) are calculated as functions of the low energy pulse duration.

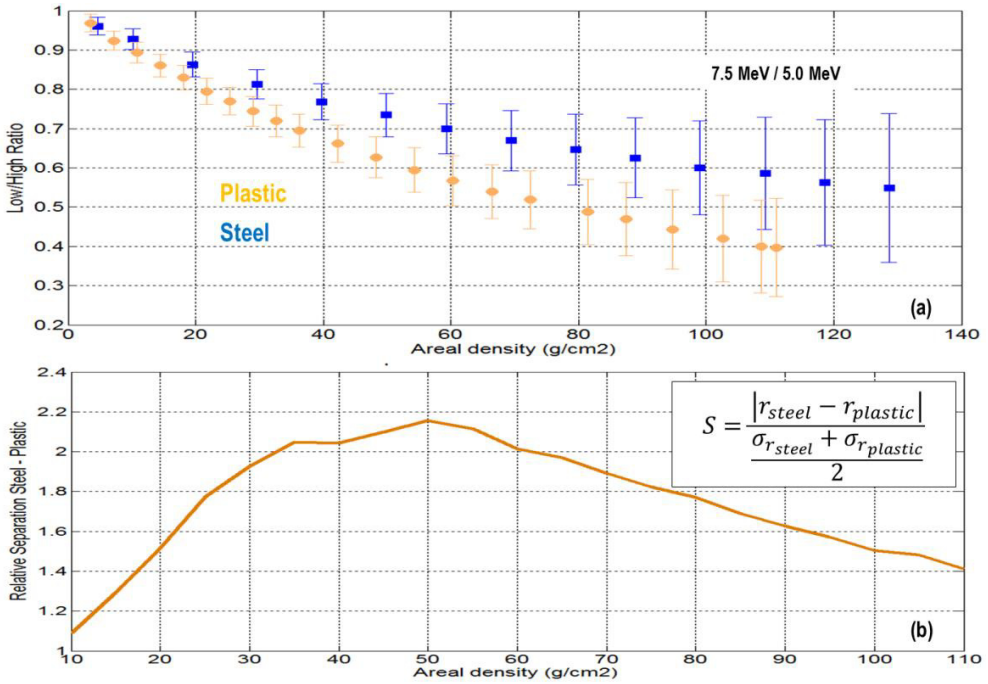

Fig. 4. Experimentally measured calibration curves for plastic (UHMW PE) and steel for a dual-energy system (a). Relative separation between the calibration curves (S) as a function of areal density (b). Larger separation translates into more accurate determination of the material, for a given areal density.

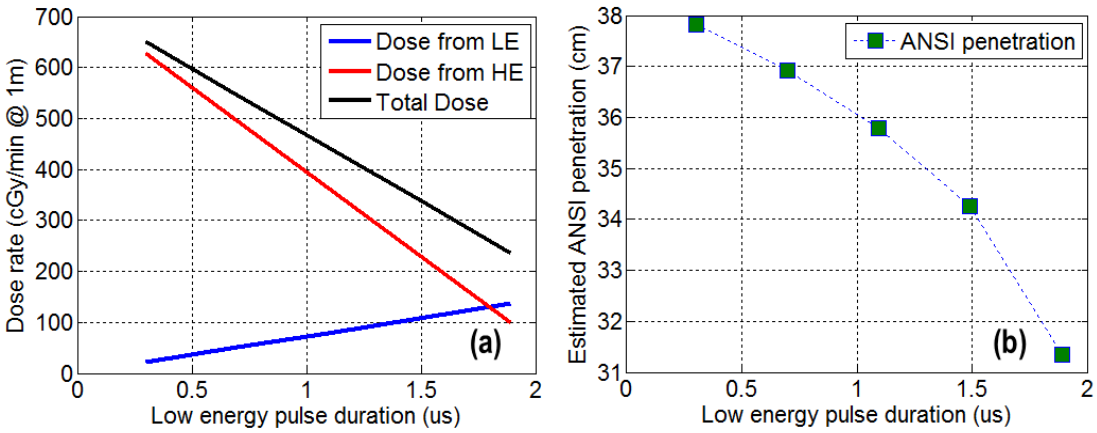

Fig. 5. Dose rate (a) and estimated ANSI penetration (b) of the system as a function of the low energy pulse duration.

Figures 5 and 6 depict the versatility of the method. For lightly loaded containers, let's say with average material areal densities below 100 g/cm^2, the low energy pulse duration can be increased to its maximum (1.89 μs). This

results in a boost in material discrimination capability (Fig. 6) and a reduction in dose-to-cargo by more than a factor of 2 (Figure 5a). The reduction in penetration to about 31 cm steel is inconsequential. The areal density corresponding to 31 cm of steel is around 240 g/cm^2, much larger than the limit of 100 g/cm^2 we chose for lightly loaded containers. When encountering optically dense objects, for which penetrating the object with X-rays is more important than getting accurate material discrimination, the duration of the low energy pulse is set to its minimum, providing the best X-ray penetration the system can offer, along with some material discrimination. In this case, the dose-to-cargo is also at its maximum. For cases in-between, automated algorithms can adjust for the best solution in terms of penetration, dose-to-cargo, and material discrimination.

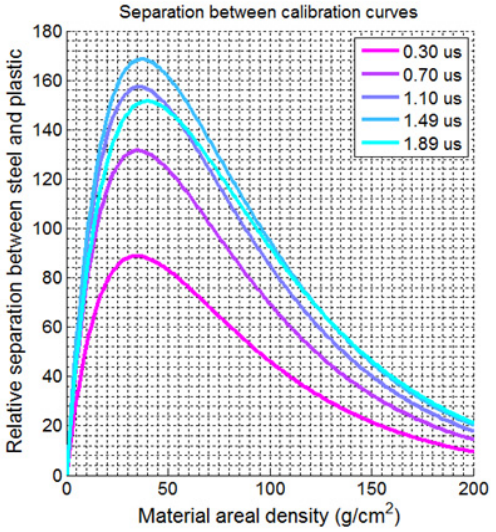

Fig. 6. Relative separation between steel and plastic (material discrimination FOM) as a function of the material areal density for different low energy pulse durations.

IPME is not limited to generating only two energies. However, simulations showed that adding more energies has quickly diminishing returns. A third, lower energy, improves the separation between plastic and steel for low attenuations, but only if the corresponding current is such that the X-ray beam flux corresponding to this component is close to the X-ray beam flux of the two higher energy components. For illustration purposes, we chose a case in which the macro-pulse has four energy components at 3, 5, 7, and 9 MeV (Figure 7). Each component has a duration of 2.5 μs and the current (Figure 7a) is chosen such that the dose per component (Figure 7b) is approximately the same for all components. The material discrimination FOM is calculated and plotted (Figure 7c) for each combination of the four energy components. For low to medium attenuations (0 – 200 g/cm^2) the 9/3 MeV combination is the best for material discrimination. Intermediate energies add dose without improving material discrimination. If the dose per macro-pulse is kept constant, it is best to use only to the 3 and 9 MeV components and discard the intermediate 5 and 7 MeV energies. For higher attenuations (>200 g/cm^2), the 5 MeV component, when paired with 9 MeV is a better option, but not by a large margin.

For realistic cases, more than two energies add dose-to-cargo without increasing the system's penetration or enhancing its ability to better discriminate among low and medium atomic number materials.

4. Summary

A novel concept of forming X-ray pulses for the IPME method of material discrimination was introduced. It allows creating sub-pulses of multiple energies with constant amplitude and enables dynamic control of the dose within each energy level. The timing conditions for forming such sub-pulses have been derived for several modes of linac operation.

Maintaining constant energy amplitudes within sub-pulses simplifies the calibration procedure and data processing for material discrimination.

A measure for material discrimination performance was introduced and a model for assessing the imaging performance was developed. The model allowed evaluating different scenarios for inspecting cargo with different densities.

Recommendations are derived for the choice of the energy-time structure of the X-ray pulse for optimizing the system performance in terms of penetration, material discrimination, and dose to cargo.

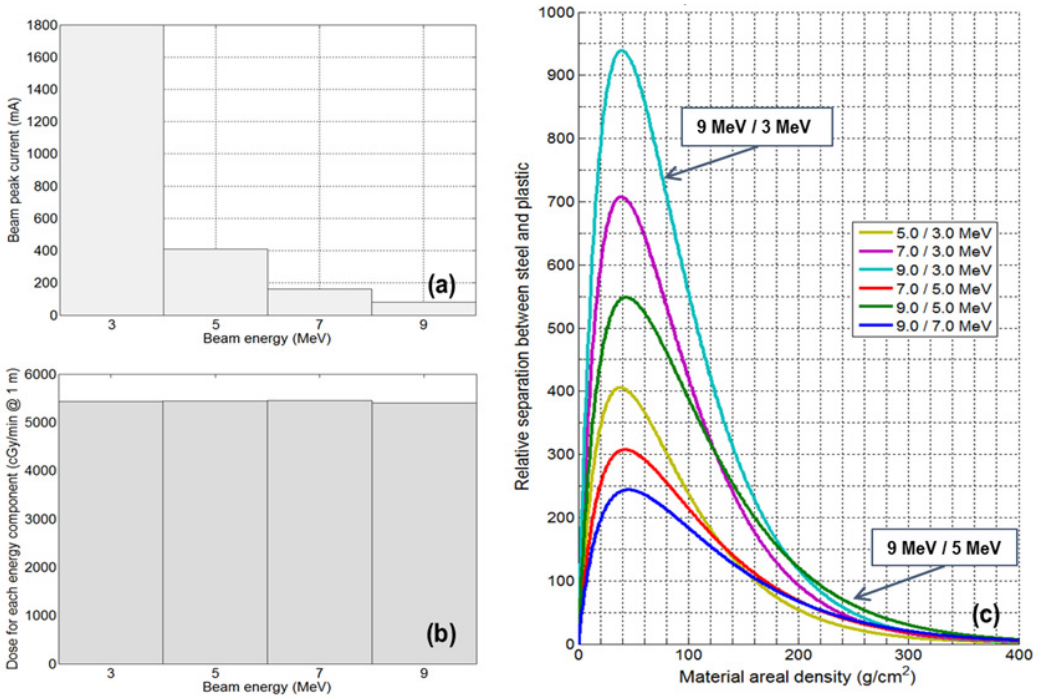

Fig. 7. Example of a four-energy component macro-pulse. The beam current (a) is chosen such that the doses for each component are approximately equal (b). The resulting pair-wise material identification FOM (c) shows the diminishing returns of adding more than two energy components.

References

Ogorodnikov, S., Petrunin, V., 2002. Processing of interlaced images in 4–10 MeV dual energy customs system for material recognition, Physical Review Special Topics - Accelerators and Beams, Volume 5, 104701.

Arodzero, A., Rommel, M., Saverskiy, A., Sud, R., 2013. System and Methods for Intra-pulse Multi-Energy and Adaptive Multi-Energy X-ray Cargo Inspection, US Patent 8,457,274 B2.

Ginzton, E. L.,1957. *Microwave Measurements*, McGraw-Hill, Inc., New York, Toronto, London.

Miller, R. H., 1986. Comparison of Standing-Wave and Traveling-Wave Structures, 1986 Linear Accelerator Conference Proceedings, Stanford, California, SLAC-Report-303, 200-205.

Sobenin, N. P., Zverev, B. V., 1999. *Electrodynamic Characteristics of Accelerating Cavities*, CRC Press.

N42.46-2008 - American National Standard for Determination of the Imaging Performance of X-Ray and Gamma-Ray Systems for Cargo and Vehicle Security Screening, Aug. 19 2008.

Liu, Y., Sowerby, B. D., Tickner J. R., 2008. Comparison of neutron and high-energy x-ray dual-beam radiography for air cargo inspection, Applied Radiation and Isotopes 66, 463-473.

Mandava, A. K., Zhang, L., Regentova, E. E., Wilson, Z., Chen, G., 2009. Radioscopic Inspection of Cargo Containers with Megavoltage Energy Barriers, Proceedings of the 2009 IEEE International Conference on Systems, Man, and Cybernetics, San Antonio, TX, USA, 3510 - 3515

Agostinelli S., et al., 2003. Geant4—a simulation toolkit, Nuclear Instruments and Methods in Physics Research Section A, Volume 506, Issue 3, 250-303.

OmniView Gantry, 2010. Retrieved from http://www.as-e.com/products-solutions/cargo-vehicle-inspection/gantry/product/omniview-gantry.